Progress In Electromagnetics Research M, Vol. 106, 153–165, 2021

A Continuous-Discontinuous Galerkin Method for Electromagnetic Simulations Based on an All-Frequency Stable Formulation

Su Yan*

Abstract—In this paper, a potential-based partial-differential formulation, called all-frequency stable formulation, is presented for the accurate and robust simulation of electromagnetic problems at all frequencies. Due to its stability from (near) dc to microwave frequencies, this formulation can be applied to simulate wide-band and multiscale problems without encountering the infamous low-frequency breakdown issue or applying basis function decompositions such as the tree-cotree splitting technique. To provide both efficient and flexible numerical solutions to the electromagnetic formulation, a mixed continuous-discontinuous Galerkin (CDG) method is proposed and implemented. In regions with homogeneous media, the continuous Galerkin method is employed to avoid the introduction of duplicated degrees of freedom (DoFs) on the elemental interfaces, while on the interfaces of two different media, the discontinuous Galerkin method is applied to permit the jump of the normal components of the electromagnetic fields. Numerical examples are provided to validate and demonstrate the proposed numerical solver for problems in a wide electromagnetic spectrum.

1. INTRODUCTION

Modeling and simulation methods of electromagnetic problems based on the numerical solution of the vector wave equation have been thoroughly investigated and widely used during the past several decades [1–5]. Many electromagnetic problems in real-world applications involve multiscale features, which are usually caused by the size differences of the geometrical structures in different parts of the objects under consideration. Typical examples include the modeling and simulation of antenna arrays, integrated circuits, and electrical machines. When applied to solve such problems, the vector wave equation, which solves for either the electric or the magnetic field intensity, breaks down due to the decoupling of these two fields. This is known to the computational electromagnetics community as the "low-frequency breakdown catastrophe," which results in erroneous solutions to the problems and must be addressed properly. Over the past few decades, two main approaches have been developed and applied to circumvent this numerical issue. One is based on the use of the vector wave equation with the separation of the mathematical representation of the electric field into the purely gradient and the rotational-like parts that correspond to the irrotational and the solenoidal components of the electric field, respectively. Through an incomplete Helmholtz decomposition, these two parts are expressed and solved with two sets of expansion functions, which leads to the first approach, the tree-cotree splitting technique [4, 6–8]. Unfortunately, the searching for the tree branches in a geometrical mesh is troublesome, especially when a multiply-connected domain is encountered. Furthermore, in the tree-cotree representation, the electric field is directly expressed, which makes it difficult to assign and handle voltage input and boundary conditions in circuit problems. The second category of approach is to formulate the electromagnetic problem in terms of the vector and scalar potentials,

Received 4 October 2021, Accepted 16 December 2021, Scheduled 22 December 2021
* Corresponding author: Su Yan (su.yan@howard.edu).
The author is with the Department of Electrical Engineering and Computer Science, Howard University, Washington, DC 20059-1015, USA.

which are then used to recover the electric and magnetic fields. This type of methods is known as the potential-based formulation and has different forms, see [9–12] and references therein. With a potential-based formulation, the vector and scalar potentials are discretized separately, which avoids the need of searching for tree branches and makes the enforcement of voltage conditions straightforward. Recently, a potential-based formulation was developed by incorporating all four Maxwell's equations and the current continuity equation [13, 14], which has been proven to be stable at all frequencies and applied to problems from dc to microwave frequencies, and hence, highly suitable for performing low-frequency and multiscale simulations. Different from the potential-based formulations developed in the past, this new formulation couples all Maxwell's equations together and is able to solve for the electric and magnetic fields in one solution, even at dc when the two fields are decoupled. This is made possible with the use of the Coulomb gauge instead of the Lorentz gauge and the introduction of an auxiliary potential. As a matter of fact, the use of the Lorentz gauge decouples the vector potential equation from the scalar potential equation. As a result, these two potentials need to be solved independently and in-tandem at dc in order to obtain both the electric and magnetic fields, as detailed in [12].

In this paper, a mixed continuous-discontinuous Galerkin (CDG) method is developed to solve the all-frequency stable formulation numerically. The discontinuous Galerkin method (DGM) [15–35] is known to be a very flexible numerical method in solving mathematical/physical equations of different types. With the use of the high-order geometrical discretization, the application of high-order basis functions, and the design of appropriate numerical fluxes, the DGM can achieve an optimal *hp* convergence, energy conservation, and spurious-free solutions. It also offers more advantages, including the flexibility of using mixed finite elements and non-conformal meshes, the use of *h*- and *p*-refinements, and the excellent parallel efficiency, all due to the use of discontinuous expansion functions [36–39]. Unfortunately, many of these flexibilities are due to the introduction of discontinuous basis functions, which doubles the number of degrees of freedom (DoFs) on the elemental interfaces. This leads to a larger system matrix to solve compared to the traditional continuous Galerkin method (CGM) such as the finite-element method [4]. It is, therefore, desirable to hybridize the DGM with the CGM to enjoy the benefits from both. In particular, in homogeneous media, CGM is used to reduce the number of DoFs and ensure field continuity, while on the interface of two different media, DGM is used to permit field discontinuity and provide numerical flexibility. Based on the idea of the interior penalty [40–43], the mixed CDG method for the all-frequency stable formulation is designed, which minimizes the total number of unknowns in a given problem while allowing the basis functions to be discontinuous wherever needed. In this paper, the proposed method will be investigated, validated, and demonstrated through the modeling and simulation of several electromagnetic problems at different frequencies.

This paper is organized as follows. The all-frequency stable formulation is introduced in Section 2. The continuous-discontinuous Galerkin method based on nodal interpolation functions is described in Section 3, and its numerical validation and application are presented in Section 4. The paper is concluded in Section 5.

2. ALL-FREQUENCY STABLE FORMULATION

The second-order wave equation for the electric field,

$$\nabla \times \mu^{-1} \nabla \times \mathbf{E} - \omega^2 \epsilon \mathbf{E} + \mathrm{j}\,\omega\sigma\mathbf{E} = -\mathrm{j}\,\omega\mathbf{J}_{\mathrm{imp}} \tag{1}$$

also known as the *E*-formulation, is very widely used to solve electromagnetic problems. In this equation, $\mathbf{E}$ denotes the electric field intensity; $\omega = 2\pi f$ denotes the angular frequency with f being frequency in Hertz; μ, ϵ, and σ stand for the material permeability, permittivity, and conductivity, respectively; and $\mathbf{J}_{\mathrm{imp}}$ stands for the impressed current density which serves as the source of the electromagnetic fields. When it is applied to solving an electromagnetic problem at low frequencies, the *E*-formulation generates erroneous numerical solutions, which is known as the low-frequency breakdown catastrophe. There are two reasons responsible for such a breakdown. First, the electric and magnetic fields are decoupled at very low frequencies, and Eq. (1) is essentially the Maxwell-Ampère's law that governs the magnetic field but expressed purely in terms of the electric field. Second, the electromagnetic sources, namely, the impressed current density $\mathbf{J}_{\mathrm{imp}}$ and the impressed charge density ρ_{imp}, which generate the magnetic and electric fields, respectively, are decoupled at low frequencies. As a result, $\mathbf{J}_{\mathrm{imp}}$ cannot generate $\mathbf{E}$ in Eq. (1) at very low frequencies.

To circumvent the breakdown problem, one can start from the original Maxwell's equations

$$\nabla \times \mathbf{E} = -\mathrm{j}\,\omega\mathbf{B} \tag{2}$$

$$\nabla \times \mu^{-1}\mathbf{B} = \mathrm{j}\,\omega\epsilon\mathbf{E} + \sigma\mathbf{E} + \mathbf{J}_{\mathrm{imp}} \tag{3}$$

$$\nabla \cdot \epsilon\mathbf{E} = \rho + \rho_{\mathrm{imp}} \tag{4}$$

$$\nabla \cdot \mathbf{B} = 0 \tag{5}$$

and the charge conservation laws that relate the impressed current and charge densities and induced current and charge densities

$$\nabla \cdot \mathbf{J}_{\mathrm{imp}} = -\mathrm{j}\,\omega\rho_{\mathrm{imp}} \tag{6}$$

$$\nabla \cdot \sigma\mathbf{E} = -\mathrm{j}\,\omega\rho. \tag{7}$$

Here the induced current density is expressed in terms of the conduction current $\mathbf{J}_c = \sigma\mathbf{E}$, and the induced charge density ρ is present only in lossy media and their boundaries.

Expressing the magnetic flux density $\mathbf{B}$ into the magnetic vector potential $\mathbf{B} = \nabla \times \mathbf{A}$, the magnetic Gauss's law in Eq. (5) is automatically satisfied. Expressing the electric field intensity $\mathbf{E}$ into the magnetic vector and the electric scalar potentials $\mathbf{E} = -\mathrm{j}\,\omega\mathbf{A} - \nabla\phi$, Faraday's law in Eq. (2) is automatically satisfied, and Maxwell-Ampère's law in Eq. (3) can be written as

$$\nabla \times \mu^{-1}\nabla \times \mathbf{A} + \mathrm{j}\,\omega\epsilon(\mathrm{j}\,\omega\mathbf{A} + \nabla\phi) + \sigma(\mathrm{j}\,\omega\mathbf{A} + \nabla\phi) = \mathbf{J}_{\mathrm{imp}}. \tag{8}$$

The remaining equations, the electric Gauss's law in Eq. (4) and the charge conservation law in Eq. (7), become

$$-\nabla \cdot (\mathrm{j}\,\omega\epsilon\mathbf{A} + \epsilon\nabla\phi) = \rho + \rho_{\mathrm{imp}} \tag{9}$$

$$-\nabla \cdot (\mathrm{j}\,\omega\sigma\mathbf{A} + \sigma\nabla\phi) = -\mathrm{j}\,\omega\rho \tag{10}$$

respectively.

To determine the vector potential $\mathbf{A}$ uniquely, a gauge condition must be imposed. In this work, the inhomogeneous Coulomb gauge is enforced implicitly, through the introduction of an auxiliary potential ψ, to yield the following complete system of equations

$$\nabla \times \mu^{-1}\nabla \times \mathbf{A} + (\mathrm{j}\,\omega\epsilon + \sigma)(\mathrm{j}\,\omega\mathbf{A} + \nabla\phi) + \epsilon\nabla\chi_0\psi = \mathbf{J}_{\mathrm{imp}} \tag{11}$$

$$-\nabla \cdot (\mathrm{j}\,\omega\epsilon\mathbf{A} + \epsilon\nabla\phi) - \rho = \rho_{\mathrm{imp}} \tag{12}$$

$$-\nabla \cdot (\mathrm{j}\,\omega\sigma\mathbf{A} + \sigma\nabla\phi) + \mathrm{j}\,\omega\rho = 0 \tag{13}$$

$$-\chi_0\nabla \cdot \epsilon\mathbf{A} - \psi = 0. \tag{14}$$

In Eqs. (11) and (14), $\chi_0 = 1/\mu_0\epsilon_0$ is chosen to balance the magnitude of the last term in Eq. (11) with respect to the first term. It is straightforward to show that the auxiliary potential ψ satisfies the inhomogeneous Laplace's equation

$$\nabla \cdot \epsilon\nabla\chi_0\psi = 0. \tag{15}$$

Together with a homogeneous Dirichlet boundary condition $\psi = 0$ on all exterior boundaries, Eq. (15) yields a trivial solution $\psi \equiv 0$, which makes Eq. (14) an implicit Coulomb gauge for the vector potential $\mathbf{A}$.

Equations (11)–(14) can be used directly to solve for the potentials $\mathbf{A}$, ϕ, and the induced charge ρ, at all frequencies. Their zero frequency behavior can be understood by setting the angular frequency $\omega = 0$, which leads to

$$\nabla \times \mu^{-1}\nabla \times \mathbf{A} + \sigma\nabla\phi + \epsilon\nabla\chi_0\psi = \mathbf{J}_{\mathrm{imp}} \tag{16}$$

$$-\nabla \cdot \epsilon\nabla\phi - \rho = \rho_{\mathrm{imp}} \tag{17}$$

$$-\nabla \cdot \sigma\nabla\phi = 0 \tag{18}$$

$$-\chi_0\nabla \cdot \epsilon\mathbf{A} - \psi = 0. \tag{19}$$

With a proper boundary condition for the scalar potential ϕ, Eqs. (17) and (18) can be solved in the lossless and lossy media, respectively, for ϕ. The induced conduction current $-\sigma\nabla\phi$ then becomes the dc current excitation for the vector potential $\mathbf{A}$ to be solved from Eqs. (16) and (19). The electrostatic and

magnetostatic fields can then be recovered as $\mathbf{E} = -\nabla\phi$ and $\mathbf{B} = \nabla \times \mathbf{A}$, respectively. Apparently, with this formulation, both the electrostatic and magnetostatic fields can be obtained in a single simulation.

The disadvantages of using Eqs. (11)–(14) directly are: 1) four sets of unknowns need to be solved and 2) the resulting system matrix is unsymmetric. These can be improved by eliminating the induced charge density ρ from Eqs. (12) and (13) to yield a symmetric system

$$\nabla \times \mu^{-1}\nabla \times \mathbf{A} - \omega^2\tilde{\epsilon}\mathbf{A} + \mathrm{j}\,\omega\tilde{\epsilon}\,\nabla\phi + \tilde{\epsilon}\,\nabla\chi_0\psi = \mathbf{J}_{\mathrm{imp}} \tag{20}$$

$$-\mathrm{j}\,\omega\nabla \cdot \tilde{\epsilon}\mathbf{A} - \nabla \cdot \tilde{\epsilon}\,\nabla\phi = \rho_{\mathrm{imp}} \tag{21}$$

$$-\chi_0\nabla \cdot \tilde{\epsilon}\mathbf{A} - \psi = 0 \tag{22}$$

which has only three sets of unknowns $\mathbf{A}$, ϕ, and ψ. In Eqs. (20) and (21), $\tilde{\epsilon} = \epsilon - \mathrm{j}\,\sigma/\omega$ is the complex permittivity. To ensure a proper normal continuity of potential $\mathbf{A}$, ϵ in ψ terms are modified to $\tilde{\epsilon}$ as well.

It should be pointed out that although the introduction of the auxiliary potential ψ term to Maxwell-Ampère's law looks similar to the penalty term in [44], which was also used to eliminate the spurious solution due to the use of nodal expansion of the vector potential $\mathbf{A}$, they are two different approaches. Indeed, the elimination of ψ in Eq. (20) using Eq. (22) yields a very similar penalty formulation as in [44]. But by retaining ψ as an independent variable, it provides the possibility of enforcing proper boundary conditions to ψ directly to suppress it in the numerical solution, hence, yields a divergence-free solution of the vector potential $\mathbf{A}$ in both homogeneous and inhomogeneous regions. Whereas in [44], the direct introduction of the penalty term into Maxwell-Ampère's law results in a solution with a lower accuracy and even erroneous solutions when discontinuous interfaces are present [45].

Equations (20)–(22) can be solved by considering the appropriate boundary conditions for electric and magnetic fields

$$\hat{\mathbf{n}} \times \mathbf{E}_1 = \hat{\mathbf{n}} \times \mathbf{E}_2, \qquad \hat{\mathbf{n}} \times \mathbf{H}_1 = \hat{\mathbf{n}} \times \mathbf{H}_2, \qquad \mathbf{r} \in \Gamma_e \tag{23}$$

$$\hat{\mathbf{n}} \times \mathbf{E} = 0, \qquad \hat{\mathbf{n}} \cdot \mathbf{H} = 0, \qquad \mathbf{r} \in \Gamma_{\mathrm{PEC}} \tag{24}$$

$$\hat{\mathbf{n}} \times \mathbf{H} = 0, \qquad \hat{\mathbf{n}} \cdot \mathbf{E} = 0, \qquad \mathbf{r} \in \Gamma_{\mathrm{PMC}} \tag{25}$$

$$\hat{\mathbf{n}} \times \mathbf{E} = -Z\hat{\mathbf{n}} \times \hat{\mathbf{n}} \times \mathbf{H}, \qquad \hat{\mathbf{n}} \times \mathbf{H} = Y\hat{\mathbf{n}} \times \hat{\mathbf{n}} \times \mathbf{E}, \qquad \mathbf{r} \in \Gamma_{\mathrm{ABC}} \tag{26}$$

where Γ_e denotes the interface between two adjacent elements; Γ_{PEC}, Γ_{PMC}, and Γ_{ABC} denote the boundaries for the perfect electric conductor (PEC), perfect magnetic conductor (PMC), and absorbing boundary condition (ABC), respectively, while Z and Y denote the intrinsic impedance and admittance of the background medium, respectively.

Applying the relations between fields and potentials, the corresponding boundary conditions for magnetic vector potential $\mathbf{A}$ and electric scalar potential ϕ, as well as those for the auxiliary potential ψ, can be expressed as follows:

(i) On the interface between two media Γ_e:

$$\hat{\mathbf{n}} \times \mathbf{A}_1 = \hat{\mathbf{n}} \times \mathbf{A}_2 \tag{27}$$

$$\hat{\mathbf{n}} \times \mu_1^{-1}\nabla \times \mathbf{A}_1 = \hat{\mathbf{n}} \times \mu_2^{-1}\nabla \times \mathbf{A}_2 \tag{28}$$

$$\hat{\mathbf{n}} \cdot \tilde{\epsilon}_1\mathbf{A}_1 = \hat{\mathbf{n}} \cdot \tilde{\epsilon}_2\mathbf{A}_2 \tag{29}$$

$$\phi_1 = \phi_2 \tag{30}$$

$$\hat{\mathbf{n}} \times \nabla\phi_1 = \hat{\mathbf{n}} \times \nabla\phi_2 \tag{31}$$

$$\hat{\mathbf{n}} \cdot \tilde{\epsilon}_1\nabla\phi_1 = \hat{\mathbf{n}} \cdot \tilde{\epsilon}_2\nabla\phi_2 \tag{32}$$

$$\psi_1 = \psi_2 \tag{33}$$

$$\hat{\mathbf{n}} \cdot \epsilon_1\nabla\psi_1 = \hat{\mathbf{n}} \cdot \epsilon_2\nabla\psi_2 \tag{34}$$

(ii) On PEC boundaries Γ_{PEC}:

$$\hat{\mathbf{n}} \times \mathbf{A} = 0 \tag{35}$$

$$\hat{\mathbf{n}} \times \nabla\phi = 0 \tag{36}$$

$$\phi = V_{\mathrm{imp}} \tag{37}$$

$$\psi = 0 \tag{38}$$

where V_{imp} stands for the impressed voltage on the voltage port.

(iii) On PMC boundaries Γ_{PMC}:

$$\hat{\mathbf{n}} \times \mu^{-1} \nabla \times \mathbf{A} = 0 \tag{39}$$

$$\hat{\mathbf{n}} \cdot \tilde{\epsilon} \mathbf{A} = 0 \tag{40}$$

$$\hat{\mathbf{n}} \cdot \tilde{\epsilon} \nabla \phi = 0 \tag{41}$$

$$\hat{\mathbf{n}} \cdot \epsilon \nabla \psi = 0 \tag{42}$$

(iv) On ABC boundaries Γ_{ABC}:

$$\phi = 0 \tag{43}$$

$$\psi = 0 \tag{44}$$

together with (26).

Equations (20)–(22) together with boundary conditions (27)–(44) form a complete system to be solved, as detailed in the coming sections.

3. CONTINUOUS-DISCONTINUOUS GALERKIN METHOD

To preserve the proper field/flux continuities, the nodal basis functions are employed to interpolate the unknown quantities, $\mathbf{A}$, ϕ, and ψ, in Eqs. (20)–(22). With the use of nodal basis functions, the CGM guarantees that all field components are continuous in homogeneous media, while DGM ensures the tangential continuity of the fields and allow the normal field components to be discontinuous.

3.1. Nodal Discontinuous Galerkin Method

When Eqs. (20)–(22) are applied across the interface of two different materials, the discontinuous Galerkin method can be used to permit the jump of normal field components across the interface. Specifically, two sets of DoFs are assigned to $\mathbf{A}$ to permit its discontinuity, while one set of DoFs is assigned to ϕ and ψ, respectively, since they are continuous even across the boundaries of two different media according to Eqs. (30) and (33).

To convert these equations into matrix equations, first denote the tetrahedral partitioning of the entire simulation domain as $V = \bigcup_{e=1}^{M} V_e$. Based on the idea of the interior penalty [40, 41], testing Eq. (20) with vector Lagrange polynomials $\mathbf{l}_i = \hat{\mathbf{u}} l_i$ in all three directions in the Cartesian coordinate system ($\hat{\mathbf{u}} = \hat{\mathbf{x}}$, $\hat{\mathbf{y}}$, or $\hat{\mathbf{z}}$) on each tetrahedral element V_e yields the discretized equation (45). Likewise, testing Eqs. (21) and (22) with scalar Lagrange polynomials l_i yield the discretized equations (46) and (47), respectively.

$$\begin{aligned}
&\int_{V_e} \left(\mu^{-1} \nabla \times \mathbf{l}_i \cdot \nabla \times \mathbf{A} - \omega^2 \tilde{\epsilon}\, \mathbf{l}_i \cdot \mathbf{A}\right) \mathrm{d}V \\
&+ \int_{\Gamma_e \bigcup \Gamma_{\mathrm{PEC}}} \left(\tau_f \left[[\mathbf{l}_i]\right] \cdot \left[[\mathbf{A}]\right] - \left\langle \mu^{-1} \nabla \times \mathbf{l}_i \right\rangle \cdot \left[[\mathbf{A}]\right] - \left[[\mathbf{l}_i]\right] \cdot \left\langle \mu^{-1} \nabla \times \mathbf{A} \right\rangle\right) \mathrm{d}S \\
&+ \mathrm{j}\,\omega Y \int_{\Gamma_{\mathrm{ABC}}} \hat{\mathbf{n}} \times \mathbf{l}_i \cdot \hat{\mathbf{n}} \times \mathbf{A} \mathrm{d}S + \mathrm{j}\,\omega \int_{V_e} \tilde{\epsilon}\, \mathbf{l}_i \cdot \nabla \phi \,\mathrm{d}V + \mu_0^{-1} \int_{V_e} \epsilon_r \mathbf{l}_i \cdot \nabla \psi \,\mathrm{d}V = \int_{V_e} \mathbf{l}_i \cdot \mathbf{J}_{\mathrm{imp}} \mathrm{d}V
\end{aligned} \tag{45}$$

$$\mathrm{j}\,\omega \int_{V_e} \tilde{\epsilon}\, \nabla l_i \cdot \mathbf{A} \mathrm{d}V + \int_{V_e} \tilde{\epsilon}\, \nabla l_i \cdot \nabla \phi \,\mathrm{d}V = \int_{V_e} l_i \rho_{\mathrm{imp}} \mathrm{d}V \tag{46}$$

$$\mu_0^{-1} \int_{V_e} \epsilon_r \nabla l_i \cdot \mathbf{A} \mathrm{d}V - \int_{V_e} l_i \psi \,\mathrm{d}V = 0 \tag{47}$$

In these equations, the average $\langle \cdot \rangle$ and jump $[[\cdot]]$ functions are defined as follows

$$\langle \mathbf{a} \rangle = 0.5(\mathbf{a}^+ + \mathbf{a}^-) \tag{48}$$

$$[[\mathbf{a}]] = \hat{\mathbf{n}}^+ \times \mathbf{a}^+ + \hat{\mathbf{n}}^- \times \mathbf{a}^- \tag{49}$$

where the superscripts $-$ and $+$ indicate the inside and outside of a surface, respectively.

In Eq. (45), τ_f denotes the interior penalty factor

$$\tau_f = \alpha \mu_f^{-1} h_f^{-1} \tag{50}$$

where h_f denotes the diameter of the circumsphere of associated tetrahedral element

$$h_f = \begin{cases} \min\{h_{f,-}, h_{f,+}\}, & f \in \Gamma_e \\ h_f, & f \in \Gamma_b \end{cases} \tag{51}$$

and

$$\mu_f = \begin{cases} \min\{\mu_{f,-}, \mu_{f,+}\}, & f \in \Gamma_e \\ \mu_f, & f \in \Gamma_b. \end{cases} \tag{52}$$

Here, Γ_b denotes all exterior boundaries. The factor $\alpha = 10p(p+1)$ with p the order of polynomials used in the expansion.

Expanding unknown quantities as

$$\mathbf{A} = \sum_{j=1}^{N} \mathbf{A}_j l_j = \sum_{j=1}^{N} \left(A_{xj}\hat{\mathbf{x}} + A_{yj}\hat{\mathbf{y}} + A_{zj}\hat{\mathbf{z}}\right) l_j \tag{53}$$

$$\phi = \sum_{j=1}^{N} \phi_j l_j, \quad \text{and} \quad \psi = \sum_{j=1}^{N} \psi_j l_j \tag{54}$$

Equations (45)–(47) can be rewritten into matrix equations

$$\begin{bmatrix} \mu^{-1}S - \omega\tilde{\epsilon}M_3 + A & \mathrm{j}\,\omega\tilde{\epsilon}D & \mu_0^{-1}\epsilon_r D \\ \mathrm{j}\,\omega\tilde{\epsilon}D^T & \tilde{\epsilon}G & 0 \\ \mu_0^{-1}\epsilon_r D^T & 0 & M_1 \end{bmatrix} \begin{Bmatrix} \mathbf{A} \\ \phi \\ \psi \end{Bmatrix} = \begin{Bmatrix} \mathbf{b}_A \\ b_\phi \\ 0 \end{Bmatrix} \tag{55}$$

where $\{\mathbf{A}\} = \{A_x, A_y, A_z\}^T$, $\{\mathbf{b}_A\} = \{b_{Ax}, b_{Ay}, b_{Az}\}^T$ with

$$[b_{Au}]_i = \int_{V_e} l_i \hat{\mathbf{u}} \cdot \mathbf{J}_{\mathrm{imp}} \mathrm{d}V \tag{56}$$

$$[b_\phi]_i = \int_{V_e} l_i \rho_{\mathrm{imp}} \mathrm{d}V. \tag{57}$$

The coefficient matrices are calculated as

$$S = \begin{bmatrix} S_{yy} + S_{zz} & -S_{yx} & -S_{zx} \\ -S_{xy} & S_{xx} + S_{zz} & -S_{zy} \\ -S_{xz} & -S_{yz} & S_{xx} + S_{yy} \end{bmatrix} \tag{58}$$

$$M_3 = \begin{bmatrix} M_1 & 0 & 0 \\ 0 & M_1 & 0 \\ 0 & 0 & M_1 \end{bmatrix} \tag{59}$$

$$A = \begin{bmatrix} 1-n_x^2 & -n_x n_y & -n_x n_z \\ -n_x n_y & 1-n_y^2 & -n_y n_z \\ -n_x n_z & -n_y n_z & 1-n_z^2 \end{bmatrix} \bigotimes M_f \tag{60}$$

$$D = \begin{bmatrix} D_x & D_y & D_z \end{bmatrix}^T \tag{61}$$

$$G = S_{xx} + S_{yy} + S_{zz} \tag{62}$$

and

$$[S_{uv}]_{ij} = \int_{V_e} \frac{\partial l_i}{\partial u} \frac{\partial l_j}{\partial v} \, \mathrm{d}V \tag{63}$$

$$[D_v]_{ij} = \int_{V_e} l_i \frac{\partial l_j}{\partial v} \, \mathrm{d}V \tag{64}$$

$$[M_1]_{ij} = \int_{V_e} l_i \, l_j \, \mathrm{d}V \tag{65}$$

$$[M_f]_{ij} = \int_{\Gamma_e} l_i \, l_j \, \mathrm{d}S. \tag{66}$$

In Eq. (60), $\bigotimes$ denotes the direct product. Note that if planar tetrahedra are used in the geometrical discretization, all the above elemental matrices have analytical expressions, regardless the order of Lagrange polynomials used [20, 33, 39, 46].

3.2. Nodal Continuous Galerkin Method

When Eqs. (20)–(22) are applied in homogeneous materials, continuous Galerkin method can be used to ensure the continuity of field components in all directions and reduce the total number of unknowns. The fully discretized equations can be obtained by enforcing the vector potential $\mathbf{A}$ to be the same across the common interface of two adjacent elements, which eliminates the surface integrals over Γ_e in Eq. (45). The matrix equation (55) thus reduces automatically to the continuous Galerkin formulation.

Assemble matrix equations in both homogeneous and inhomogeneous regions of the simulation domain yield the complete system of equations, which can be solved for $\mathbf{A}$, ϕ, and ψ. The electric and magnetic field can then be recovered by

$$\mathbf{E} = -\mathrm{j}\,\omega\mathbf{A} - \nabla\phi \tag{67}$$

$$B = \nabla \times \mathbf{A}. \tag{68}$$

4. NUMERICAL EXAMPLES

Three numerical examples are given in this section to demonstrate the application of the proposed formulation and numerical method.

4.1. Scattering from a PEC Cylinder

In the first example, electromagnetic scattering from an infinite length PEC cylinder is calculated, in both the TM and the TE cases. This example is designed to test the implementation of the PEC, PMC, and ABC boundary conditions in the CDG method and demonstrate the application of the all-frequency stable formulation at a microwave frequency. In this example, a square region with a small depth is considered. The width and length of the region are both 10 m, and the depth 0.1 m. Sitting in the center of the simulation domain, the PEC cylinder has a radius of 1 m. The PEC boundary condition is specified on the surface of the cylinder, the PMC boundary condition is specified on both surfaces in the depth direction, and the ABC boundaries are used around the square region to supply incident plane wave and absorb scattering wave from the cylinder. Using such boundary conditions, the essentially 2-D problem is simulated in 3-D, where a 300-MHz plane wave incidents from the left boundary and illuminates the cylinder. At 300 MHz, the simulation domain is discretized into tetrahedral elements with an average size of 0.05 m, resulting in 1, 238, 158 elements and 1, 238, 025 nodal unknowns (A_x, A_y, A_z, ϕ, and ψ). In this example, the entire air region is a CG region and only the PEC, PMC, and ABC boundaries are DG regions. Shown in Figs. 1(a) and 1(c) are the snapshots of the z components of the total electric field and magnetic flux in the TM and the TE cases, respectively. The near field distributions E_z in the TM case and H_z in the TE case are recorded along a circle with a radius of 3 m from the center of the cylinder and compared with the analytical Mie series solutions in Figs. 1(b) and 1(d), respectively. From these figures, a very good near field accuracy is observed. Apparently, the potential-based formulation can be applied to the microwave frequency regime correctly, which validates its application to wave propagation and scattering problems at a relatively high frequency.

4.2. A Simple RC Circuit

In the second example, a simple first-order RC circuit is considered to demonstrate the application of the all-frequency stable formulation and the associated CDG method in resistive and capacitive regions. Shown in Fig. 2, the blue traces stand for metallic wires with conductivity $\sigma = 10^6$ S/m, the red block stands for a resistor with a resistivity $\varrho = 6 \times 10^5\,\Omega$-m, and the yellow rectangle stands for a dielectric material with a relative permittivity $\epsilon_r = 10$ sandwiched between the parallel plates of a capacitor. The

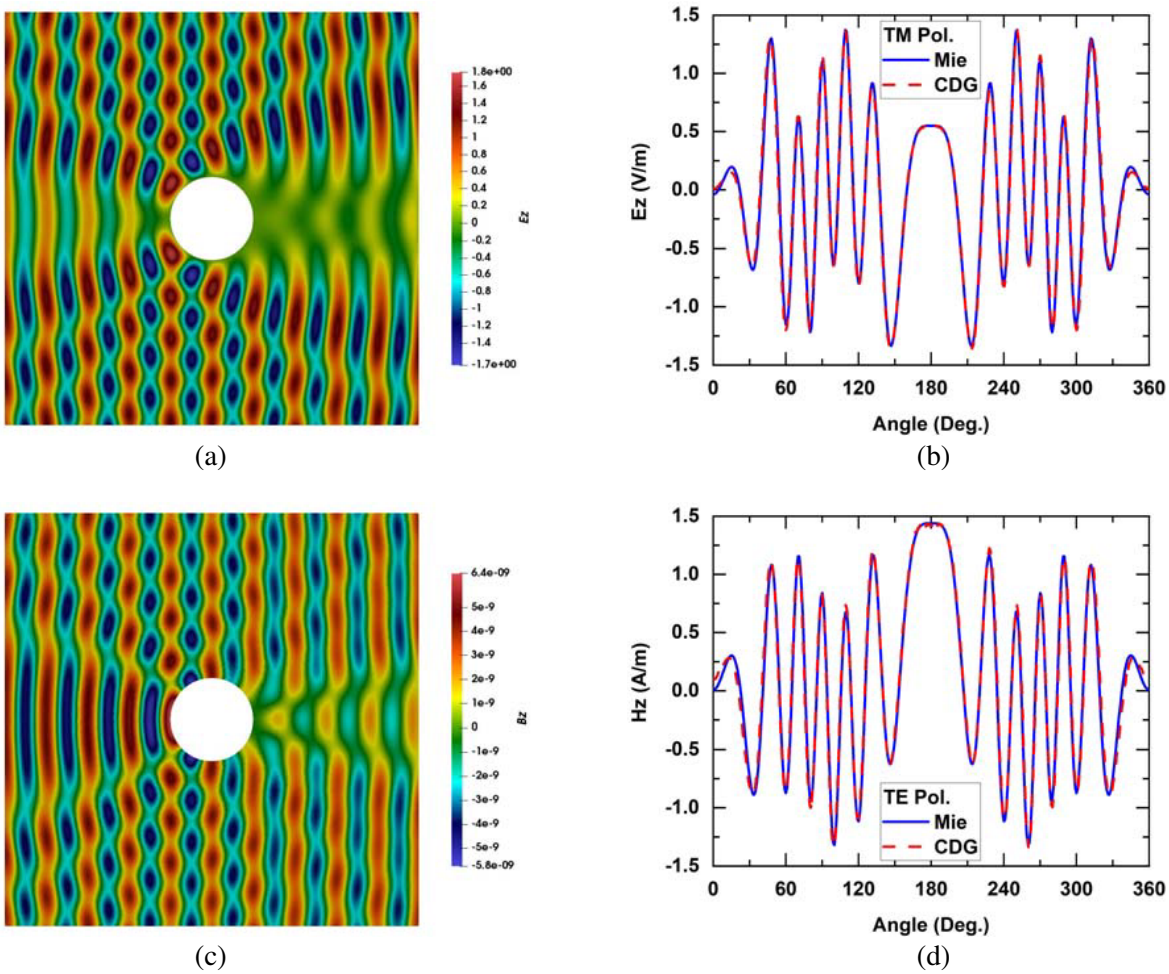

Figure 1. Scattering by a circular conducting cylinder with a radius of 1λ. (a) Snapshot of the total field E_z in 2-D; (b) Comparison of E_z obtained from the proposed method and the Mie series; (c) Snapshot of the total field B_z in 2-D; (d) Comparison of H_z obtained from the proposed method and the Mie series.

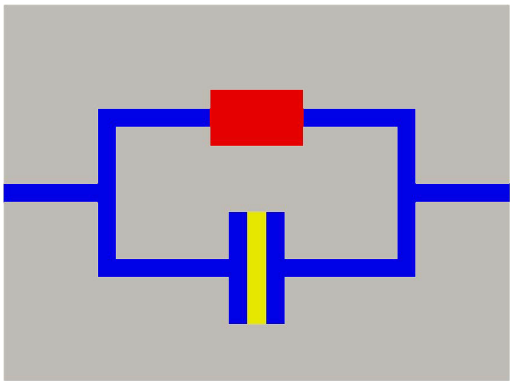

Figure 2. Circuit configuration. The width of the traces is 1 cm.

right terminal of the metal wire is grounded, and the left terminal is connected to a 1-V voltage source operating at 1 Hz, 1 kHz, 10 kHz, and 100 kHz. The total size of the simulation domain is 27 cm by 20 cm by 0.2 cm, and the width of the metallic trace is 1 cm. To resolve the skin depth at higher frequencies,

tetrahedra with an average size of 0.1 cm are used to discretize the simulation domain, resulting in a total of 1, 094, 553 elements and 1, 231, 644 nodal unknowns in this example. The CGM is applied in air, metallic, resistor, and capacitor regions, while the DGM is applied on the interfaces between all the CGM regions and over the external boundaries. The electric field, magnetic field, and conduction current distributions are presented in Fig. 3, where the solutions at different frequencies are presented in four columns from the left to the right. It is very interesting to see that at 1 Hz, the current flows through the resistor only, since the capacitor is an open circuit at such a low frequency. The conduction current presented in Fig. 3(i) generates the magnetic flux that follows Biot-Savart's law, as can be seen clearly in Fig. 3(e). As the frequency increases, the current starts to flow through the lower branch of the circuit, and the skin effect starts to present. At 100 kHz, the majority of current flows through the capacitor in terms of the displacement current.

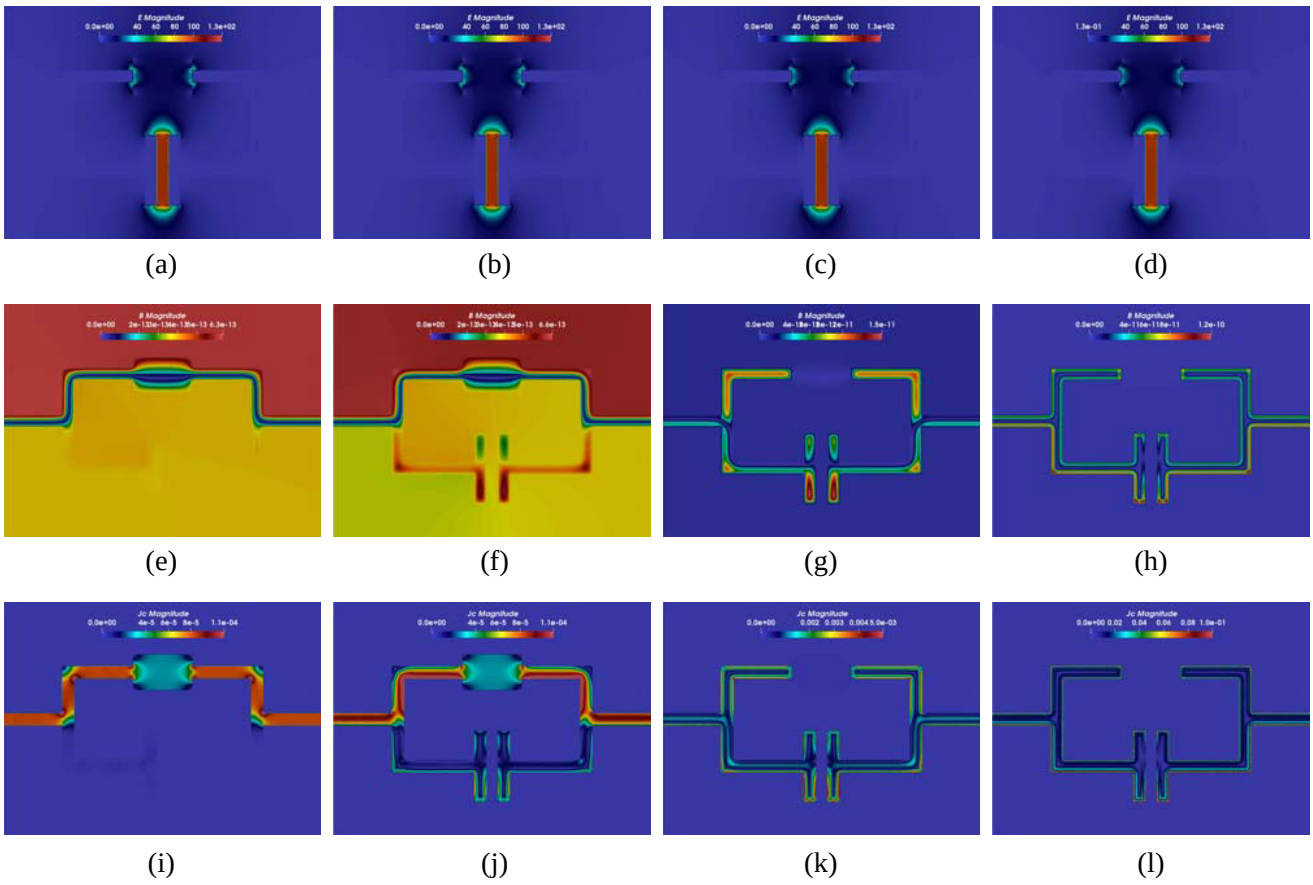

Figure 3. First row: electric field distribution; Second row: magnetic field distribution; Third row: conduction current distribution. Four columns from the left to the right: results at 1 Hz, 1 kHz, 10 kHz, and 100 kHz.

4.3. A Coil Inductor

As a third example, a coil inductor is simulated at different frequencies to demonstrate the application of the all-frequency stable formulation and the associated CDG method in inductive regions. As shown in Fig. 4, the inductor is made of a magnetic core with $\mu_r = 1000$ and a 26-turn metallic wire with a diameter of 1.2 mm and conductivity $\sigma = 10^6$ S/m. A 1-V voltage source is connected to the upper terminal of the wire, while the lower terminal is grounded. This inductor is simulated at four different frequencies, 0 Hz, 50 Hz, 50 kHz, and 5 MHz, with the proposed formulation and method. The total size of this simulation domain is 50 mm by 50 mm by 40 mm. The mesh sizes for the coil winding, the

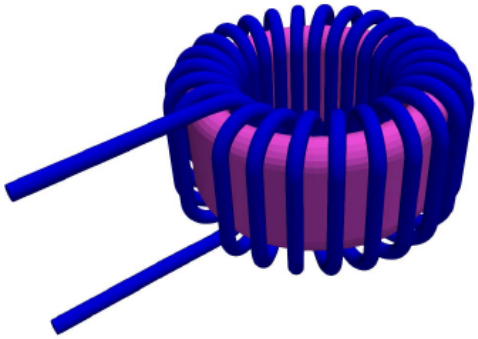

Figure 4. Coil inductor configuration. The diameter of the metallic wire is 1.2 mm.

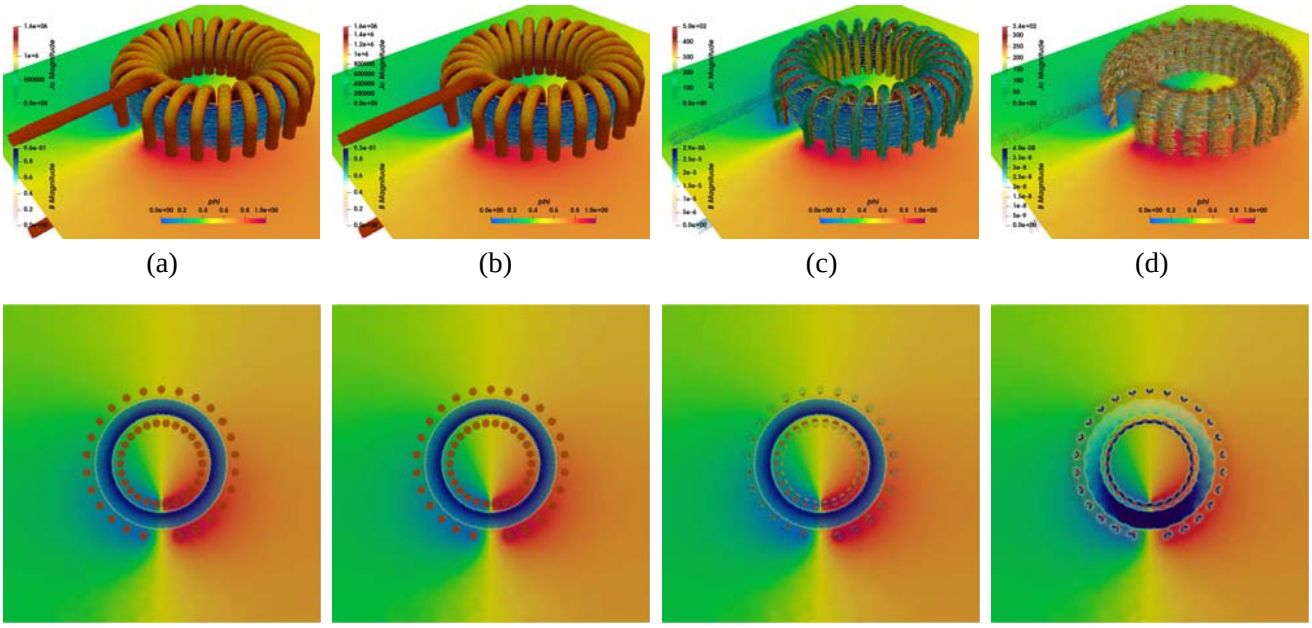

Figure 5. First row: distributions of conduction current, magnetic flux, and electric scalar potential; Second row: horizontal cut. Four columns from the left to the right: results at 0 Hz, 50 Hz, 50 kHz, and 5 MHz.

magnetic core, and the air regions are 0.2 mm, 0.5 mm, and 2 mm, respectively. This leads to a total of 669,098 elements and 619,012 nodal unknowns. In each homogeneous region, the CGM is applied and on the material interfaces and external boundaries, the DGM is applied. The simulation results are shown in Fig. 5, where the conduction current $\mathbf{J}_c = \sigma\mathbf{E}$ and magnetic flux $\mathbf{B}$ are presented in 3-D in the first row, and are shown in a 2-D cut across the center plane in the second row. In both rows, the electric scalar potential ϕ distribution on the cutting plane is shown. Columns from the left to the right correspond to simulation results at different frequencies. From these results, it can be seen that at lower frequencies, 0 and 50 Hz, the conduction currents distribute uniformly in the metallic wire, which generate uniform and strong magnetic fluxes inside the magnetic core. The magnetic fluxes circulating in the magnetic core store magnetic energy, which makes the structure an efficient inductor as is normally used in low-frequency circuits. On the contrary, from the simulation results obtained at higher frequencies, 50 kHz and 5 MHz, the conduction currents and the resulting magnetic fluxes start to distribute non-uniformly, due to the presence of the skin effect at higher frequencies. As a result, less magnetic energy can be stored in the core, and the structure does not perform as an efficient inductor any more.

5. CONCLUSION

In this paper, an all-frequency formulation has been shown to be stable at all frequencies both theoretically and numerically. Due to the use of electric scalar and magnetic vector potentials, this formulation requires no special treatment to avoid the low-frequency breakdown problem. A mixed continuous-discontinuous Galerkin method has been proposed to solve such a formulation numerically to provide continuous solutions in homogeneous materials and discontinuous solutions across the interface of material discontinuity. Based on the presented numerical examples, it is clear that the proposed formulation and method are able to capture the electromagnetic behaviors in a very wide frequency range. The method proposed in this paper has a promising potential to solve other problems involving wide-band or multiscale characteristics. With the application of nodal polynomial basis functions, the nodal CDG method is extremely attractive in problems that concern normal field/current components, such as the accurate extraction of circuit parameters and the multiphysics simulations involving interactions between fields and charges.

ACKNOWLEDGMENT

This work was supported in part by NSF Award 2101012 and in part by DOE NETL Award DE-FE0032092.

REFERENCES

1. Taflove, A., *Computational Electrodynamics: The Finite-Difference Time-Domain Method*, Artech House, Norwood, MA, 1995.
2. Harrington, R. F., *Field Computation by Moment Methods*, Macmillan, New York, NY, USA, 1968.
3. Jin, J.-M., *Theory and Computation of Electromagnetic Fields*, Wiley, Hoboken, NJ, USA, 2010.
4. Jin, J.-M., *The Finite Element Method in Electromagnetics*, 3rd Edition, Wiley, Hoboken, NJ, 2014.
5. Chew, W. C., J.-M. Jin, E. Michielssen, and J. M. Song, *Fast and Efficient Algorithms in Computational Electromagnetics*, Artech House, Norwood, MA, USA, 2001.
6. Manges, J. B. and Z. J. Cendes, "Tree-cotree decompositions for first-order complete tangential vector finite elements," *Int. J. Numer. Methods Eng.*, Vol. 40, 1667–1685, 1997.
7. Albanese, R. and G. Rubinacci, "Solution of three dimensional eddy current problems by integral and differential methods," *IEEE Trans. Magn.*, Vol. 24, 98–101, Jan. 1998.
8. Lee, S.-C., J.-F. Lee, and R. Lee, "Hierarchical vector finite elements for analyzing waveguiding structures," *IEEE Trans. Microw. Theory Techn.*, Vol. 51, No. 8, 1897–1905, Aug. 2003.
9. Badics, Z. and J. Pávó, "Full wave potential formulation with low-frequency stability including ohmic losses," *IEEE Trans. Magn.*, Vol. 51, No. 3, 7402204, Mar. 2015.
10. Dyczij-Edlinger, R., G. Peng, and J.-F. Lee, "A fast vector-potential method using tangentially continuous vector finite elements," *IEEE Trans. Microw. Theory Techn.*, Vol. 46, No. 6, 863–868, 1998.
11. Li, Y.-L., S. Sun, Q. I. Dai, and W. C. Chew, "Finite element implementation of the generalized-Lorenz gauged A-Φ formulation for low-frequency circuit modeling," *IEEE Trans. Antennas Propag.*, Vol. 64, No. 10, 4355–4364, Oct. 2016.
12. Chew, W. C., "Vector potential electromagnetics with generalized gauge for inhomogeneous media: Formulation," *Progress In Electromagnetics Research*, Vol. 149, 69–84, 2014.
13. Zhao, Y. and W. N. Fu, "A new stable full-wave Maxwell solver for all frequencies," *IEEE Trans. Magn.*, Vol. 53, No. 6, 7200704, Jun. 2017.
14. Yan, S., "All-frequency stable potential-based formulation for electromagnetic modeling and simulation," *Proc. IEEE Antennas Propag. Symp.*, Atlanta, GA, USA, Jul. 2019.

15. Dumbser, M., M. Käser, and E. F. Toro, "An arbitrary high-order discontinuous Galerkin method for elastic waves on unstructured meshes — V. Local time stepping and p-adaptivity," *Geophys. J. Int.*, Vol. 171, 695–717, 2007.
16. Cockburn, B., G. E. Karniadakis, and C.-W. Shu, "The development of discontinuous Galerkin methods," *Discontinuous Galerkin Methods: Theory, Computation and Applications (Lecture Notes in Computational Science and Engineering)*, Vol. 11, 3–50, Springer-Verlag, New York, NY, USA, 2000.
17. Zhang, M. and C.-W. Shu, "An analysis of three different formulations of the discontinuous Galerkin method for diffusion equations," *Math. Models Methods Appl. Sci.*, Vol. 13, No. 3, 395–413, Mar. 2003.
18. Cockburn, B. and C. W. Shu, "Runge-Kutta discontinuous Galerkin methods for convection dominated problems," *J. Sci. Comput.*, Vol. 16, 173–261, 2001.
19. Cockburn, B. and C.-W. Shu, "The local discontinuous Galerkin method for time-dependent convection-diffusion systems," *SIAM J. Numer. Anal.*, Vol. 35, 2440–2463, 1998.
20. Hesthaven, J. S. and T. Warburton, *Nodal Discontinuous Galerkin Methods: Algorithms, Analysis, and Applications*, Springer, New York, 2008.
21. Descombes, S., C. Durochat, S. Lanteri, L. Moya, C. Scheid, and J. Viquerat, "Recent advances on a DGTD method for time-domain electromagnetics," *Photonics and Nanostructures — Fundamentals and Applications*, Vol. 11, 291–302, 2013.
22. Lu, T., P. W. Zhang, and W. Cai, "Discontinuous Galerkin methods for dispersive and lossy Maxwell's equations and PML boundary conditions," *J. Comput. Physics*, Vol. 200, No. 2, 549–580, Nov. 2004.
23. Gedney, S. D., C. Luo, J. A. Roden, R. D. Crawford, B. Guernsey, J. A. Miller, T. Kramer, and E. W. Lucas, "The discontinuous Galerkin finite-element time-domain method solution of Maxwell's equations," *Applied Comput. Electromag. Society J.*, Vol. 24, No. 2, 129–142, Apr. 2009.
24. Xiao, T. and Q. H. Liu, "Three-dimensional unstructured-grid discontinuous Galerkin method for Maxwell's equations with well-posed perfectly matched layer," *Microwave Opt. Technol. Lett.*, Vol. 46, No. 5, 459–463, 2005.
25. Chen, J., Q. H. Liu, M. Chai, and J. A. Mix, "A non-spurious 3-D vector discontinuous Galerkin finite-element time-domain method," *IEEE Microw. Wireless Compon. Lett.*, Vol. 20, No. 1, 1–3, Jan. 2010.
26. Tobón, L. E., Q. Ren, and Q. H. Liu, "A new efficient 3D discontinuous Galerkin time domain (DGTD) method for large and multiscale electromagnetic simulations," *J. Computat. Phys.*, Vol. 283, 374–387, Feb. 2015.
27. Li, P. and L. J. Jiang, "A hybrid electromagnetics-circuit simulation method exploiting discontinuous Galerkin finite element time domain method," *IEEE Microw. Wireless Compon. Lett.*, Vol. 23, No. 3, 113–115, Mar. 2013.
28. Li, P., Y. F. Shi, L. J. Jiang, and H. Bağci, "A hybrid time-domain discontinuous Galerkin-boundary integral method for electromagnetic scattering analysis," *IEEE Trans. Antennas Propag.*, Vol. 62, No. 5, 2841–2816, May 2014.
29. Alvarez, J., L. D. Angulo, M. F. Pantoja, A. R. Bretones, and S. G. Garcia, "Source and boundary implementation in vector and scalar DGTD," *IEEE Trans. Antennas Propag.*, Vol. 58, No. 6, 1997–2003, Jun. 2010.
30. Alvarez, J., L. D. Angulo, A. R. Bretones, and S. G. Garcia, "A spurious-free discontinuous Galerkin time-domain method for the accurate modeling of microwave filters," *IEEE Trans. Microw. Theory Techn.*, Vol. 60, No. 8, 2359–2369, Aug. 2012.
31. Angulo, L. D., J. Alvarez, M. F. Pantoja, S. G. Garcia, and A. R. Bretones, "Discontinuous Galerkin time domain methods in computational electrodynamics: State of the art," *FERMAT: Forum for Electromagnetic Research Methods and Application Technologies*, Vol. 10, 1–24, Aug. 2015.
32. Chen, G., L. Zhao, W. Yu, S. Yan, K. Zhang, and J.-M. Jin, "A general scheme for the DGTD modeling and S-parameter extraction of inhomogeneous waveports," *IEEE Trans. Microw. Theory Techn.*, Vol. 66, No. 4, 1701–1712, Apr. 2018.

33. Yan, S., A. D. Greenwood, and J.-M. Jin, "Modeling of plasma formation during high-power microwave breakdown in air using the discontinuous Galerkin time-domain method (invited paper)," *IEEE J. Multiscale and Multiphys. Comput. Techn.*, Vol. 1, 2–13, Jun. 2016.
34. Yan, S., A. D. Greenwood, and J.-M. Jin, "Simulation of high-power microwave air breakdown modeled by a coupled Maxwell-Euler system with a non-Maxwellian EEDF," *IEEE Trans. Antennas Propag.*, Vol. 66, No. 4, 1882–1893, Apr. 2018.
35. Chang, C.-P., G. Chen, S. Yan, and J.-M. Jin, "Waveport modeling for the DGTD simulation of electromagnetic devices," *Int. J. Numer. Model. El.*, 1–9, Feb. 2017.
36. Klöckner, A., T. Warburton, J. Bridge, and J. S. Hesthaven, "Nodal discontinuous Galerkin methods on graphics processors," *J. Comput. Phys.*, Vol. 228, No. 21, 7863–7882, 2009.
37. Baumann, C. E. and J. T. Oden, "A discontinuous hp finite element method for convection-diffusion problems," *Comput. Methods Appl. Mech. Engrg.*, Vol. 175, 311–341, 1999.
38. Yan, S., C.-P. Lin, R. R. Arslanbekov, V. I. Kolobov, and J.-M. Jin, "A discontinuous Galerkin timedomain method with dynamically adaptive Cartesian meshes for computational electromagnetics," *IEEE Trans. Antennas Propag.*, Vol. 65, No. 6, 3122–3133, Jun. 2017.
39. Yan, S. and J.-M. Jin, "A dynamic p-adaptive DGTD algorithm for electromagnetic and multiphysics simulations," *IEEE Trans. Antennas Propag.*, Vol. 65, No. 5, 2446–2459, May 2017.
40. Arnold, D. N., F. Brezzi, B. Cockburn, and L. D. Marini, "Unified analysis of discontinuous Galerkin methods for elliptic problems," *SIAM J. Numer. Anal.*, Vol. 39, No. 5, 1749–1779, 2002.
41. Tian, C.-Y., Y. Shi, and C. H. Chan, "Interior penalty discontinuous Galerkin time-domain method based on wave equation for 3-D electromagnetic modeling," *IEEE Trans. Antennas Propag.*, Vol. 65, No. 12, 7174–7184, 2017.
42. Tian, C.-Y., Y. Shi, and C. H. Chan, "An improved vector wave equation-based discontinuous Galerkin time domain method and its hybridization with Maxwell's equation-based discontinuous Galerkin time domain method," *IEEE Trans. Antennas Propag.*, Vol. 66, No. 11, 6170–6178, 2018.
43. Yang, Q., Y. Shi, Z. G. Ban, and S. C. Zhu, "A nodal discontinuous Galerkin time-domain method based on wave equation," *IEEE Antennas Wireless Propag. Lett.*, Vol. 19, No. 7, 1083–1087, 2020.
44. Coulomb, J. L., "Finite element three dimensional magnetic field computation," *IEEE Trans. Magn.*, Vol. 17, 3241–3246, 1981.
45. Demerdash, N. A. and R. Wang, "Theoretical and numerical difficulties in 3-D vector potential methods in finite element magnetostatic computations," *IEEE Trans. Magn.*, Vol. 26, 1656–1658, 1990.
46. Yan, S. and J.-M. Jin, "A continuity-preserving and divergence-cleaning algorithm based on purely and damped hyperbolic Maxwell equations in inhomogeneous media," *J. Comput. Phys.*, Vol. 334, 392–418, Apr. 2017.